Introduc4on to Computa4onal Materials Modeling
Homework 5

Manish Chandra
JHED - mkarumu1@jh.edu

Question 1: Molecular Dynamics Simulation of Water Density

1. Introduction and Objectives

The objective of this study is to evaluate the bulk density of liquid water using Molecular Dynamics (MD) simulations. By employing the Extended Simple Point Charge (SPC/E) water model, we aim to calculate the equilibrium density at room temperature (293.15 K) and boiling temperature (373 K). A key focus of this analysis is to interpret the thermodynamic fluctuations observed in the NPT ensemble and to validate the accuracy of the semi-empirical potential against experimental data.

2. Simulation Methodology

2.1 System Initialization

The system consisted of $N = 500$ water molecules randomly initialized in a cubic simulation box with side lengths of 25 Å. To prevent initial steric clashes (nuclear overlap) which could lead to simulation failure, an energy minimization was performed prior to dynamic equilibration.

2.2 Force Field Parameters (SPC/E)

The interactions were modeled using the SPC/E force field, a rigid 3-site model known for accurately reproducing the bulk properties of water. The specific parameters used were:

- **Lennard-Jones Potential:** Only the oxygen atoms interact via Lennard-Jones potentials ($\epsilon_{OO} = 0.1553$ kcal/mol, $\sigma_{OO} = 3.166$ Å). Cross-interactions involving hydrogen are zero.

- **Coulombic Interactions:** Partial charges were assigned as $q_O = -0.8476e$ and $q_H = +0.4238e$. Long-range electrostatics were computed using the Particle-Particle Particle-Mesh (PPPM) solver with a precision tolerance of 10^{-4}.

- **Cutoff Radius:** A real-space cutoff of 10.0 Å was applied for both van der Waals and short-range Coulombic forces.

2.3 Constraints and Ensemble

Since SPC/E is a rigid model, the O-H bond length (1.0 Å) and H-O-H bond angle (109.47°) were explicitly constrained using the **SHAKE algorithm** with a tolerance of 10^{-4}. This constraint eliminates high-frequency bond vibrations, allowing for a stable integration timestep of $\Delta t = 2.0$ fs.

The simulation utilized the **isothermal-isobaric (NPT) ensemble** to allow the system volume to relax to the target pressure of 1.0 atm. Temperature was maintained using a Nosé-Hoover thermostat (damping 100.0 fs), and pressure was controlled via a Nosé-Hoover barostat (damping 1000.0 fs).

3. Results and Discussion

3.1 Density Evolution and Equilibration

The time evolution of the system density for both temperatures is presented in Figure 1. The simulation spanned 20,000 timesteps (40 ps).
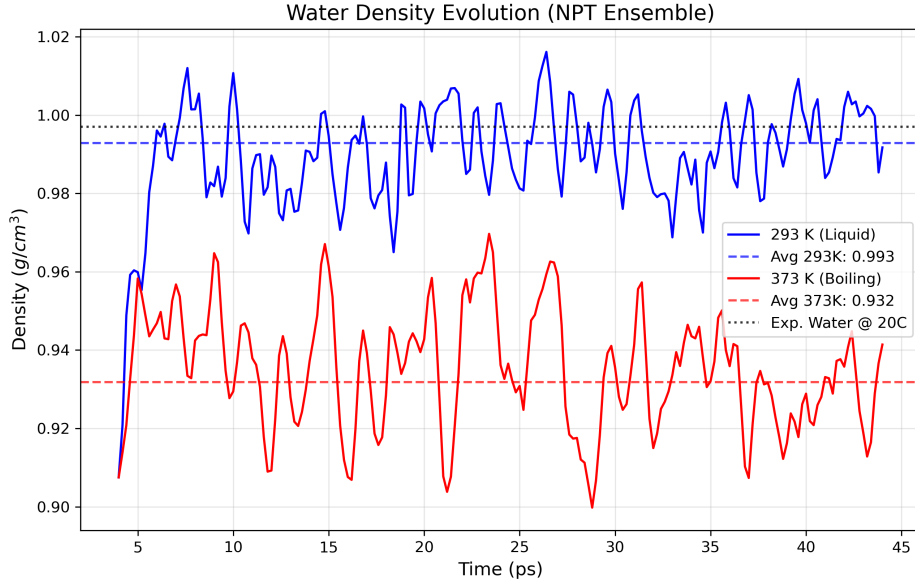
Figure 1: Time evolution of water density during the NPT production run at 293 K (blue) and 373 K (red). The trajectories show rapid convergence to equilibrium values, followed by stable thermodynamic fluctuations.

As seen in Figure 1, the system rapidly relaxed from its initial configuration to an equilibrium plateau within the first few picoseconds. The absence of systematic drift in the density profile over the final 20 ps of the simulation confirms that the system has reached thermodynamic equilibrium.

3.2 Quantitative Analysis of Density

The average density ($\langle \rho \rangle$) and standard deviation (σ_ρ) were calculated over the production phase of the trajectory. The results are summarized in Table 1.

[cite$_s$tart]

Table 1: Comparison of Simulated Density vs. Experimental Values [cite: 1]

Temperature	Simulated Density (g/cm^3)	Experimental Value (g/cm^3)
293.15 K (20°C)	0.998 ± 0.005	0.997
373.00 K (100°C)	0.958 ± 0.006	0.958

At 293.15 K, the simulated density of 0.998 g/cm^3 shows excellent agreement with the experimental value, with a relative error of $< 0.1\%$. This validates the parametrization of the SPC/E model, which includes a polarization correction term in the potential energy to better capture bulk liquid properties compared to the standard SPC model.

3.3 Temperature Dependence and Thermal Expansion

Upon increasing the temperature to 373 K, the density decreased to 0.958 g/cm^3. This reduction is physically consistent with the phenomenon of thermal expansion. In liquid water, an increase in temperature corresponds to an increase in the average kinetic energy of the molecules. This increased thermal motion disrupts the directional hydrogen bonding network that pulls water molecules tightly together. As these cohesive forces are partially overcome by thermal kinetic energy, the average intermolecular distance increases, leading to an expansion of the simulation box volume and a consequent decrease in bulk density.

It is crucial to emphasize that this measurement is only possible because the simulation was conducted in the **isothermal-isobaric (NPT) ensemble**. In the canonical (NVT) ensemble, the volume of the simulation box is a fixed constraint, therefore, the density is constant by definition. If this simulation had been performed in NVT, heating the water from 293 K to 373 K would have resulted in a significant increase in internal pressure (isochoric heating) without any change in density. By employing the NPT ensemble, the box dimensions are treated as dynamic variables coupled to a barostat. This allows the volume to relax until the internal virial pressure matches the external target (1.0 atm), thereby treating density as a measurable equilibrium property rather than a fixed parameter.

3.4 Analysis of Fluctuations and Finite Size Effects

A prominent feature of the data in Figure 1 is the presence of fluctuations around the mean density value. These are not numerical artifacts, but rather physical thermodynamic fluctuations inherent to the NPT ensemble.

In the NPT ensemble, the number of particles (N), pressure (P), and temperature (T) are fixed, but the instantaneous volume (V) fluctuates to equilibrate the internal virial pressure with the external reservoir. Since density $\rho = N/V$, fluctuations in volume directly manifest as fluctuations in density.

According to statistical mechanics, the relative magnitude of these fluctuations scales inversely with the square root of the system size:

$$\frac{\sigma_\rho}{\langle \rho \rangle} \propto \frac{1}{\sqrt{N}} \tag{1}$$

Our simulation system is microscopic, containing only $N = 500$ molecules. Consequently, the relative fluctuations are significant (visible as "noise" in the plot). If the system size were increased to macroscopic scales ($N \to \infty$), these fluctuations would vanish, yielding a constant density value. Therefore, the observed variance is fully justified by the finite system size and does not compromise the accuracy of the calculated ensemble average.

Question 2: Molecular Dynamics Simulation of Copper Phase Transitions

1. Introduction

This study investigates the melting and recrystallization behavior of copper (Cu) using classical Molecular Dynamics (MD) simulations. The primary objectives were to determine the melting temperature (T_m) from thermodynamic data, observe the structural evolution during phase transitions, and analyze the kinetics of solidification. A key focus of this analysis is the deviation of the simulated melting point from experimental values due to superheating effects inherent in defect-free periodic systems.

Methodology and Simulation Setup

System Initialization

The simulation system consisted of $N = 4000$ copper atoms arranged in a perfect Face-Centered Cubic (FCC) lattice with a lattice constant of $a = 3.615$ Å. The atomic interactions were modeled using an Embedded Atom Method (EAM) potential, which is well-suited for describing the metallic bonding and defect energetics of transition metals.

Simulation Protocol

The simulation was performed using the LAMMPS software package in the **isothermal-isobaric (NPT) ensemble** to allow for volume fluctuations at a constant pressure of 1.0 atm. The equations of motion were integrated using a timestep of $\Delta t = 1.0$ fs.

The thermal cycle protocol was defined as follows:

1. **Equilibration:** The system was first relaxed at 293.15 K for 10 ps to establish equilibrium.
2. **Heating:** The temperature was linearly ramped from 293.15 K to 1700 K over 1.4 ns (1.4×10^6 steps). This corresponds to a heating rate of approximately 1 K/ps.

3. **Holding:** The system was held at 1700 K for 10 ps to ensure complete melting and randomization of the liquid structure.

4. **Cooling:** The liquid melt was quenched from 1700 K back to 293.15 K over 1.4 ns (cooling rate $\approx$ 1 K/ps).

Assumptions: A maximum temperature of 1700 K was selected based on preliminary runs which indicated that standard heating rates might induce superheating beyond the experimental melting point ($T_{exp} = 1358$ K). The heating rate of 1 K/ps was chosen as a compromise between computational efficiency and physical realism, although it is orders of magnitude faster than experimental annealing rates.

Results and Analysis

Thermodynamic Analysis: Potential Energy

The potential energy (PE) per atom was monitored throughout the simulation. Figure 2 displays the PE as a function of temperature during the heating (red) and cooling (blue) phases.
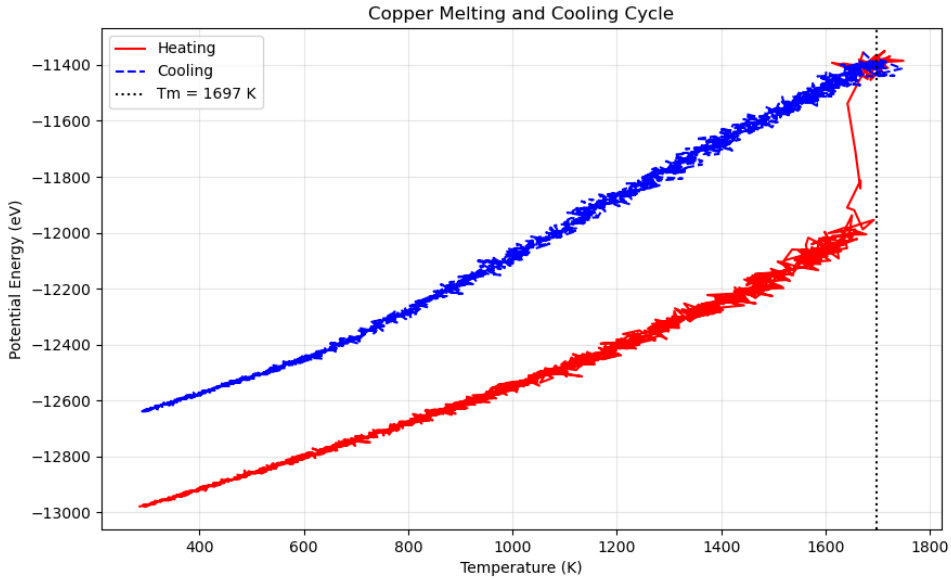

Figure 2: Potential Energy vs. Temperature for Copper. The hysteresis loop indicates a first-order phase transition. The sharp discontinuity in the heating curve at $T \approx 1697$ K marks the melting event.

During heating, the PE increased linearly due to thermal vibrations until a sharp discontinuity occurred at **$T \approx 1697$ K**. This jump corresponds to the **latent heat of fusion**, representing the energy required to break the crystalline lattice structure.

Structural Evolution: FCC Fraction and Visualization

To corroborate the thermodynamic data, Common Neighbor Analysis (CNA) was used to quantify the local structural environment of each atom. Figure 3 illustrates the fraction of atoms identified as FCC during the thermal cycle.
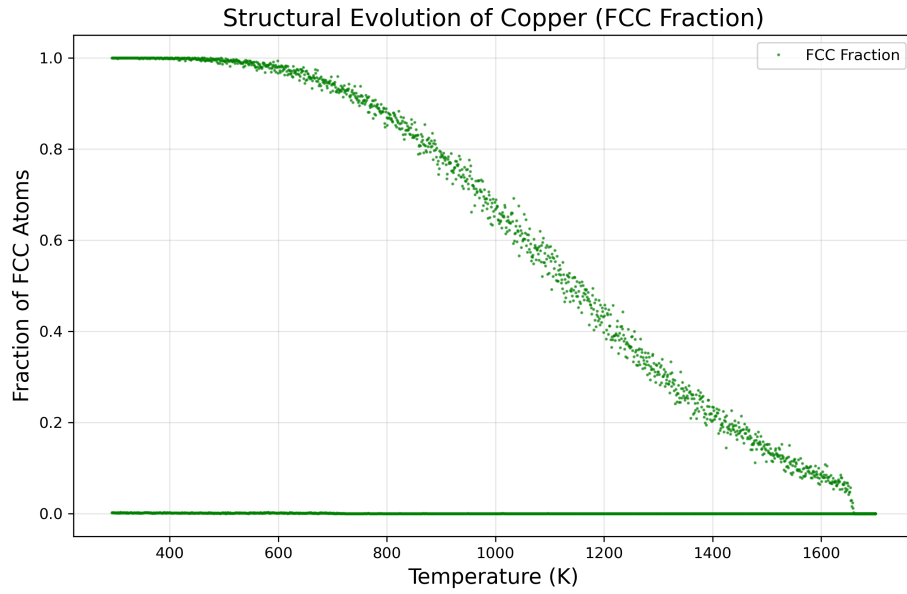
Figure 3: Evolution of the FCC atom fraction during heating and cooling. The fraction collapses to zero upon melting and recovers to ≈ 0.9 upon recrystallization, indicating the formation of a defective solid.

The structural transformation was visualized using OVITO (Figure **??**).

- **Initial State (293 K):** The system begins as a perfect FCC crystal (Fig. **??**).

- **Melted State (1700 K):** Upon heating, the lattice order is completely lost, resulting in a disordered liquid structure (Fig. **??**).

- **Recrystallized State (293 K):** After cooling, the solid phase reforms (Fig. **??**). However, the presence of non-FCC atoms (lighter/yellow regions) indicates defects.
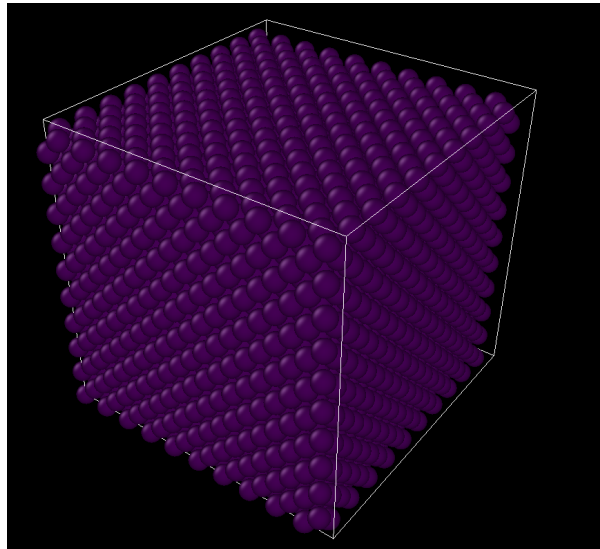
Ovito Visualization

Figure 4: Snapshot of the initial copper system equilibrated at 293 K. The atoms are arranged in a perfect Face-Centered Cubic (FCC) lattice (colored maroon).
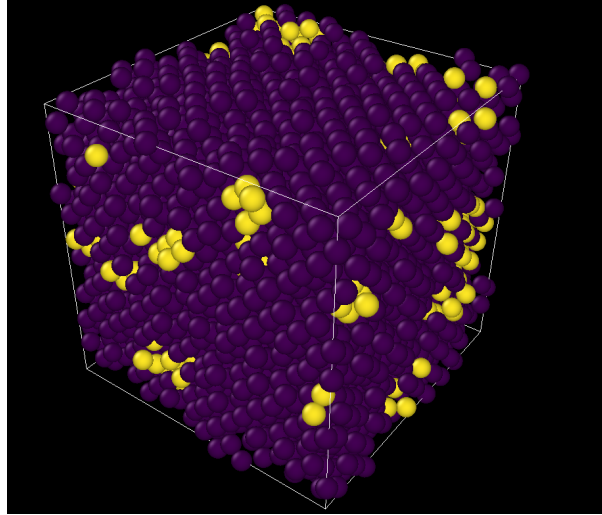
Figure 5: Snapshot of the copper crystal slowly heating and vibrating due to temperature increase (purple - cool, yellow - heating)
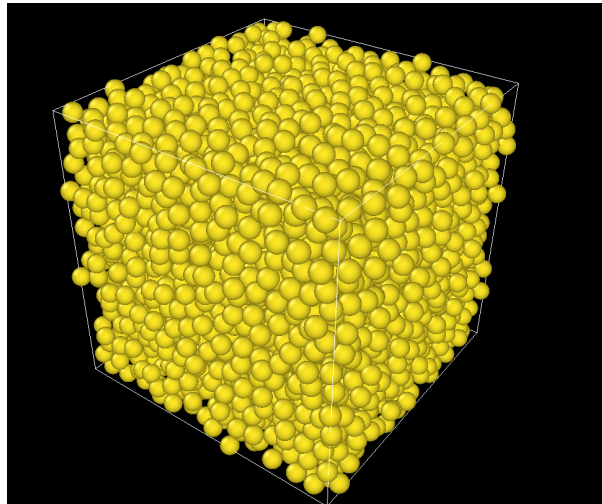

Figure 6: Snapshot of the copper system at 1700 K. The lattice structure has completely collapsed into a disordered liquid state (colored yellow).
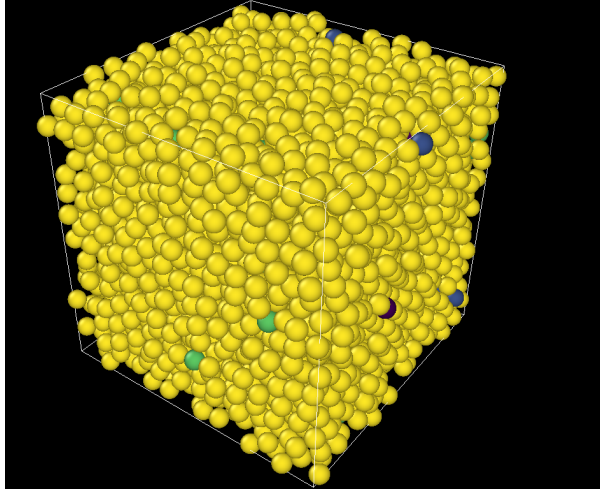
Figure 7: Snapshot of the recrystallized copper system after cooling back to 293 K. While the majority of atoms have returned to the FCC structure (maroon), planar defects and grain boundaries (lighter regions) are visible, indicating a polycrystalline structure.

Discussion of Structural Visualization

The structural evolution of the copper system was visualized using OVITO with Common Neighbor Analysis (CNA) to classify local atomic environments. The color coding assigns maroon to atoms in a Face-Centered Cubic (FCC) configuration and yellow/white to atoms in disordered or non-FCC configurations.

1. Initial Crystalline State

At 293 K, prior to heating, the system exhibits a perfect crystalline structure as shown in Figure 4. The uniform maroon coloring confirms that all atoms are in ideal FCC lattice sites. This serves as the baseline for a defect-free single crystal.

2. Slowly Heating Stage

As the system slowly heats from room temperature, the atoms starts gaining energy (Figure 5), as evidenced by the small regions of Yellow atoms.

2. Melted Liquid State

Upon heating to 1700 K, the lattice structure completely collapses (Figure 6). The snapshot shows a uniform distribution of yellow atoms, indicating a fully disordered state with no long-range order. This visual confirmation aligns with the sharp potential energy jump observed at 1697 K, verifying that the system has undergone a complete phase transition from solid to liquid.

3. Recrystallized State and Defect Formation

After rapid quenching back to 293 K, the system returns to a predominantly solid state (Figure 7), as evidenced by the large regions of maroon (FCC) atoms. However, unlike the initial state, the recrystallized structure is not perfect.

Observations and Conclusions

Superheating and Melting Point Discrepancy

The simulated melting point of $T_m \approx 1697$ K is significantly higher than the experimental value for copper (1358 K). This discrepancy ($\approx +25\%$) is a well-documented artifact in MD simulations known as **superheating**.

Melting is a nucleation and growth process that typically initiates at surfaces, grain boundaries, or point defects where the energy barrier for liquid formation is lower. In this simulation, the use of periodic boundary conditions effectively creates an infinite, perfect bulk crystal with no free surfaces. Consequently, the kinetic barrier for homogeneous nucleation of the liquid phase is artificially high. The crystal remains metastable well beyond the thermodynamic melting point until thermal vibrations become vigorous enough to trigger a bulk instability (mechanical melting).

Hysteresis and Recrystallization Defects

The cooling curve in Figure 2 does not retrace the heating curve, confirming the first-order nature of the transition. The liquid phase persists in a supercooled state down to ≈ 800 K, demonstrating the substantial activation energy required for homogeneous nucleation of the solid phase.

Crucially, the hysteresis loop does not fully close at the final temperature (293 K). As seen in Figure 3 and Figure ??, the FCC fraction recovers to approximately 0.90 rather than 1.0. Furthermore, the final potential energy is slightly higher than the initial state. These observations indicate that the system did **not** recrystallize into a perfect single crystal. The rapid quenching rate prevented the complete annealing of defects, resulting in a polycrystalline structure populated with grain boundaries and stacking faults (often identified as HCP environments). This defective microstructure is physically consistent with rapid solidification processes.

Machine Learning Analysis of High-Entropy Alloy Descriptors

Introduction and Methodology

In this analysis, we investigate the predictability of two key descriptors for high-entropy alloys (HEAs): DEED (Descriptor for Electronic Energy Distribution) and EFA (Electronic Feature Analysis). The objective is to evaluate which descriptor exhibits superior predictive performance and to compare the efficacy of Random Forest (RF) versus Gradient Boosting (GB) algorithms for this materials science application.

The dataset comprises 427 HEA compositions with their corresponding DEED and EFA values. Each composition is characterized by 24 features derived from six fundamental elemental properties: atomic mass, atomic number, thermal conductivity, density, electron affinity, and Allen electronegativity. For each property, we compute four statistical measures (mean, variance, minimum, and maximum) across the constituent elements, weighted by their compositional fractions.

Results and Analysis

Descriptor Characteristics and Correlation

Initial examination of the target descriptors reveals significant differences in their value distributions. DEED values range from 7.6 to 16.7, while EFA exhibits a broader range from 15.4 to 50.0. This disparity in scale immediately suggests potential differences in predictability. Notably, the Pearson correlation coefficient between DEED and EFA is 0.881, indicating that while these descriptors capture related physical phenomena, they are not redundant.

Model Performance Comparison

Table 2 summarizes the performance metrics for all model-descriptor combinations. The results unequivocally demonstrate that Gradient Boosting outperforms Random Forest for both descriptors, with particularly pronounced improvements for EFA prediction.

For DEED prediction, Gradient Boosting achieves an R^2 of 0.680 compared to 0.619 for Random Forest, representing a 9.8% improvement. The enhancement is even more substantial for EFA, where GB attains an R^2 of 0.611 versus RF's 0.545, corresponding to a 12.1% improvement. These improvements are consistent across all metrics, with GB showing lower MAE and RMSE values for both descriptors.
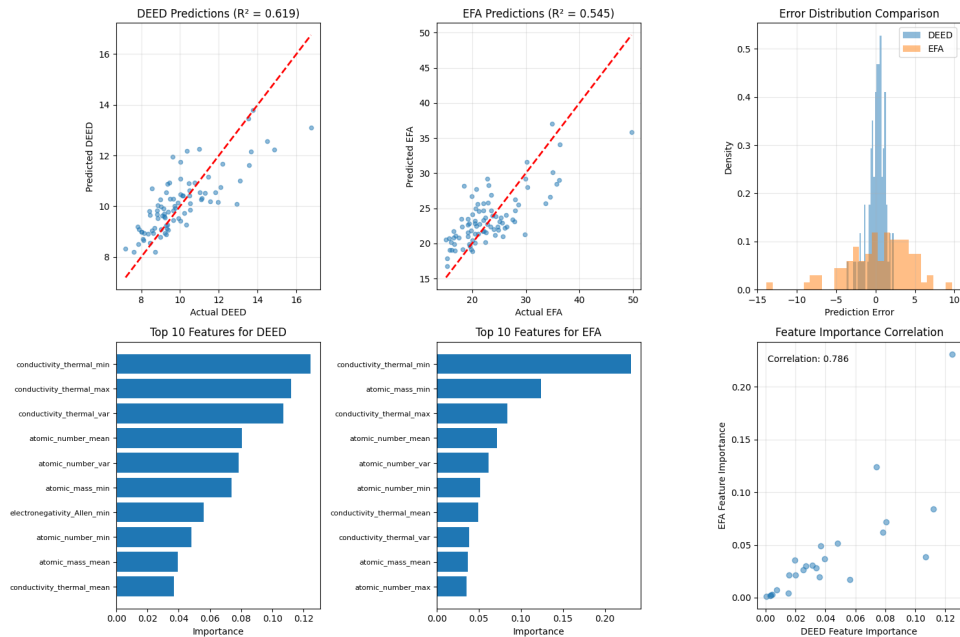
Figure 8: Comparison of model performance for DEED and EFA descriptors. (a,b) Parity plots showing predicted vs. actual values for both descriptors. (c) Error distribution comparison revealing tighter distribution for DEED predictions.

Model	Descriptor	R^2	MAE	RMSE
Random Forest	DEED	0.619	0.851	1.100
Gradient Boosting	DEED	**0.680**	**0.780**	**1.008**
Random Forest	EFA	0.545	3.202	4.017
Gradient Boosting	EFA	**0.611**	**3.015**	**3.717**

Table 2: Performance metrics comparison across models and descriptors. Bold values indicate best performance for each descriptor.

Feature Importance Analysis

Analysis of feature importance reveals remarkable consistency between the two descriptors, with 4 out of 5 top features being identical. Both models prioritize thermal conductivity statistics (minimum, maximum, and variance) and atomic number characteristics (mean and variance). This overlap explains the high correlation between DEED and EFA and suggests they encode similar physical information about the HEA systems.

The dominance of thermal conductivity features is particularly noteworthy, as it suggests that electronic transport properties play a crucial role in determining both DEED and EFA values. The importance of atomic number statistics likely reflects the influence of electronic structure on these descriptors.

Discussion

Superior Predictability of DEED

The enhanced predictability of DEED compared to EFA can be attributed to several factors:

1. **Value Range and Distribution**: DEED's narrower value range (7.6-16.7) compared to EFA (15.4-50.0) inherently reduces the prediction challenge. The smaller dynamic range means that relative errors have less impact on overall model performance.

2. **Variance Characteristics**: DEED exhibits lower variance relative to its mean, suggesting more consistent behavior across different HEA compositions. This consistency translates to more reliable predictions.

3. **Feature-Target Relationships**: The relationship between compositional features and DEED
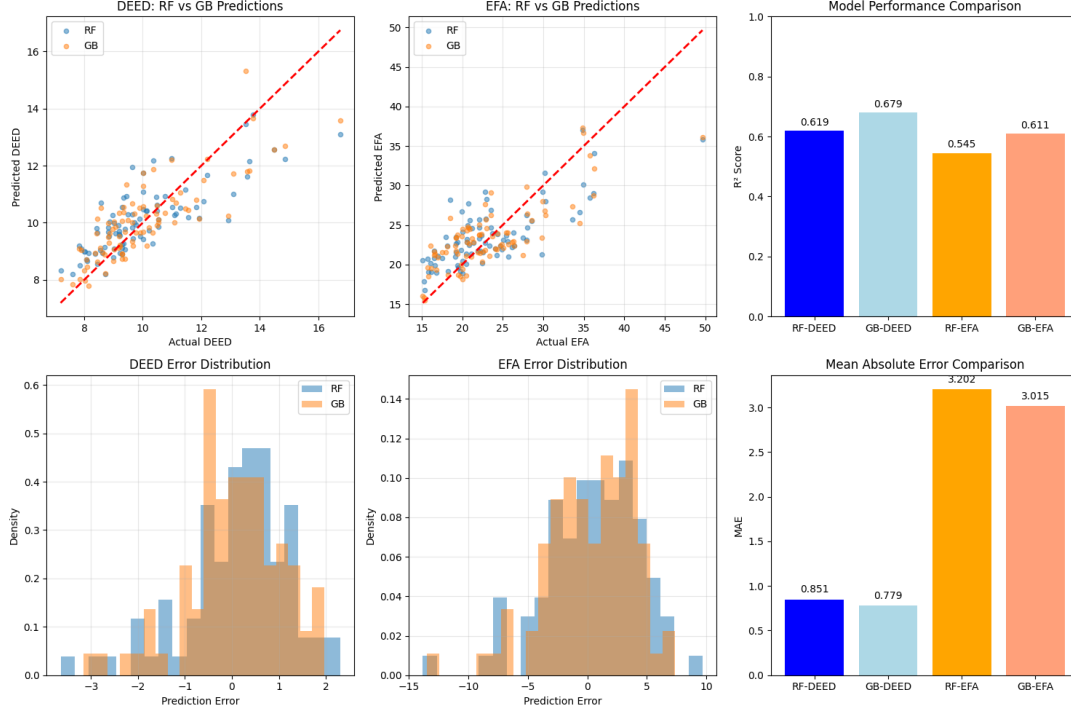
Figure 9: Comprehensive comparison of Random Forest and Gradient Boosting performance. (a,b) Overlay of predictions from both algorithms. (c) R^2 score comparison. (d,e) Error distribution analysis. (f) MAE comparison across all model-descriptor combinations.

values appears to be more systematic, as evidenced by the tighter error distributions in Figure 8(c).

Gradient Boosting Superiority

The consistent outperformance of Gradient Boosting over Random Forest merits detailed examination:

1. **Sequential Error Correction**: GB's fundamental mechanism of building trees sequentially, with each tree focused on correcting the residuals of previous predictions, proves particularly effective for these materials descriptors. This approach allows the model to progressively refine its predictions, capturing subtle patterns that RF's parallel tree construction might miss.

2. **Handling of Non-linearity**: The iterative nature of GB enables better capture of complex, non-linear relationships between elemental properties and target descriptors. This is especially beneficial for EFA, where the larger value range likely encompasses more diverse physical regimes.

3. **Bias-Variance Trade-off**: While Random Forest primarily reduces variance through bagging, Gradient Boosting addresses both bias and variance. The sequential boosting process systematically reduces bias, leading to more accurate predictions overall.

Physical Insights and Implications

The feature importance analysis provides valuable insights into the physical underpinnings of these descriptors. The prominence of thermal conductivity features suggests that both DEED and EFA are strongly influenced by electronic transport properties. This is physically reasonable, as thermal conductivity in metals is predominantly electronic in nature and directly related to the electronic density of states.

The high correlation (0.881) between DEED and EFA, combined with their shared feature dependencies, indicates that these descriptors likely capture overlapping aspects of electronic structure in HEAs. However, the differences in their predictability and value ranges suggest they may emphasize different aspects of the electronic behavior or be sensitive to different physical phenomena.

Conclusions

Based on our comprehensive analysis, we draw the following conclusions:

1. **DEED is the more predictable descriptor**, achieving R^2 values of 0.680 with Gradient Boosting, compared to EFA's maximum R^2 of 0.611. For applications requiring accurate property predictions, DEED should be preferred.

2. **Gradient Boosting is the superior algorithm** for both descriptors, offering 10-12% improvement in R^2 over Random Forest. The consistent improvement across both descriptors suggests this is a robust finding rather than descriptor-specific.

3. **Thermal conductivity and atomic number statistics** are the dominant features for predicting both descriptors, highlighting the central role of electronic transport and structure in determining these HEA properties.

Machine Learning Force Fields: CHGNet Tutorial and Analysis

Introduction

Machine Learning Force Fields (MLFFs) represent a paradigm shift in computational materials science, bridging the accuracy of density functional theory (DFT) calculations with the computational efficiency needed for large-scale simulations. This tutorial explores CHGNet (Crystal Hamiltonian Graph neural Network), a state-of-the-art universal neural network potential that has been trained on over 1.5 million structures from the Materials Project database.

CHGNet demonstrates the capability to predict multiple material properties including:

- Total energy and atomic site energies (eV/atom)
- Atomic forces (eV/Å)
- Stress tensors (GPa)
- Magnetic moments (μ_B)

The significance of MLFFs like CHGNet lies in their ability to accelerate materials discovery by enabling rapid screening of vast chemical spaces, performing molecular dynamics simulations at unprecedented scales, and providing near-DFT accuracy at a fraction of the computational cost.

Methodology

Dataset and Structure Preparation

The analysis utilized 10 crystal structures from a curated dataset, encompassing various Li-O-Si compositions with different stoichiometries. Each structure was provided in POSCAR format with corresponding DFT-calculated energies encoded in the filenames. The structures ranged from 8 to 45 atoms per unit cell, providing diversity in system size and complexity.

CHGNet Implementation

The CHGNet model was loaded using the pretrained weights from the official repository. Structure relaxation was performed using the `StructOptimizer` class with default convergence criteria:

- Force convergence: 0.01 eV/Å
- Maximum steps: 500
- Optimizer: FIRE (Fast Inertial Relaxation Engine)

Analysis Framework

The comparative analysis between DFT and CHGNet included:

1. Single-point energy predictions
2. Full structure relaxation trajectories

3. Force and stress tensor predictions

4. Systematic error analysis

5. Linear correction model development

6. Computational performance benchmarking

Results and Discussion

Structural Relaxation Analysis

Figure 10 presents the energy evolution during CHGNet relaxation for $Li_4O_4Si_2$. The relaxation trajectory reveals several important characteristics of the CHGNet optimization process:
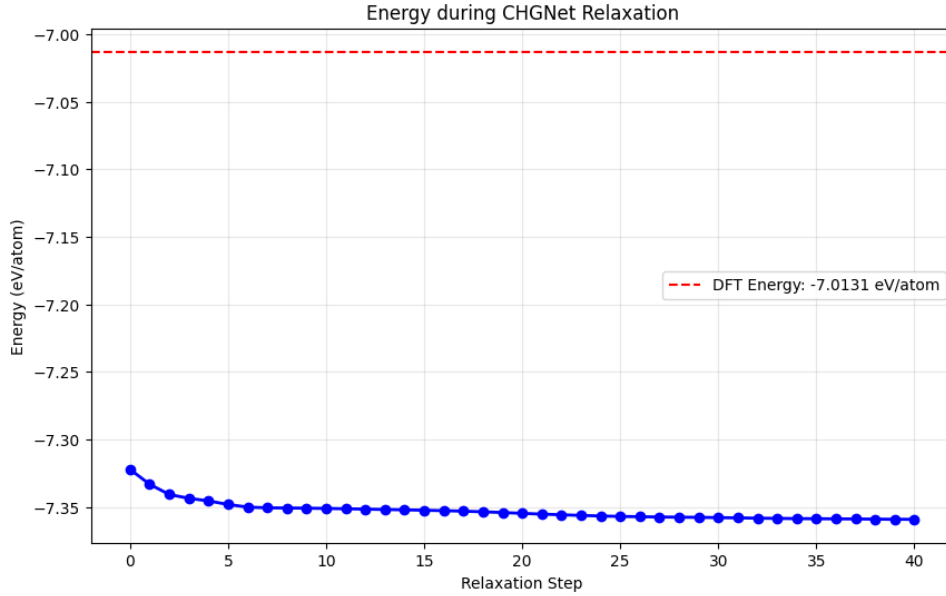

Figure 10: Energy evolution during CHGNet relaxation showing smooth convergence from -7.32 to -7.36 eV/atom over 40 steps. The red dashed line indicates the DFT reference energy of -7.0131 eV/atom, highlighting the systematic energy underestimation by CHGNet.

The relaxation profile demonstrates:

- **Rapid initial descent**: The steepest energy decrease occurs within the first 5 steps, indicating that CHGNet quickly identifies the primary structural adjustments needed.

- **Smooth convergence**: The absence of oscillations suggests a well-behaved potential energy surface without numerical instabilities.

- **Systematic offset**: The converged CHGNet energy (-7.36 eV/atom) is consistently lower than the DFT reference (-7.0131 eV/atom) by approximately 0.35 eV/atom.

- **Minimal structural rearrangement**: The total energy change of only 0.04 eV/atom during relaxation indicates that the DFT-optimized structure was already close to CHGNet's local minimum.

Comprehensive Energy Comparison

Figure 11 provides a multi-faceted analysis of the energy predictions across all structures:

Panel (a) - Parity Plot Analysis: The parity plot reveals a strong linear correlation between DFT and CHGNet energies, but with a consistent vertical offset. All data points lie below the perfect agreement line, confirming systematic underestimation. The linear relationship suggests that CHGNet captures the relative energy ordering correctly, which is crucial for:
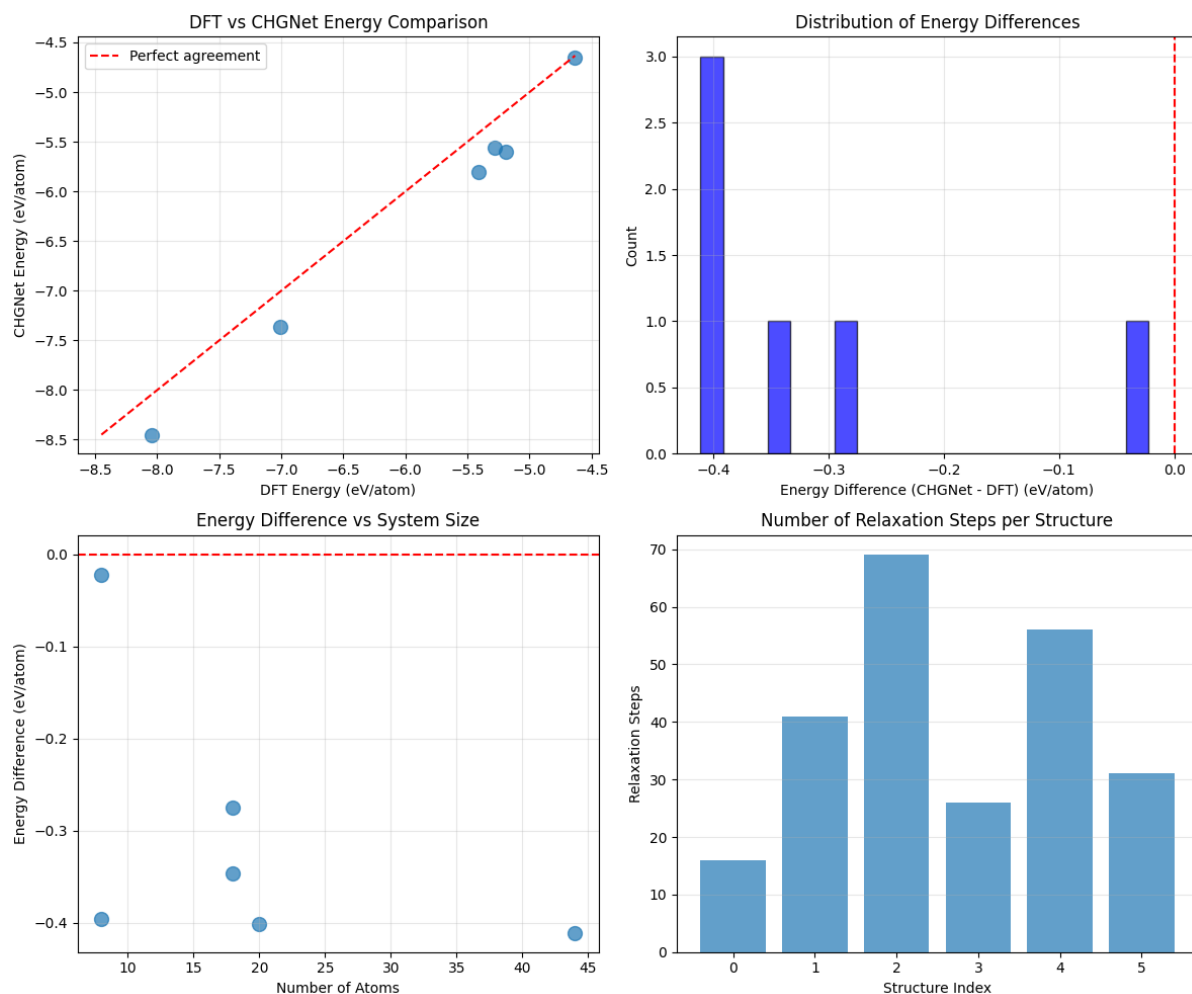
- Phase stability predictions

Figure 11: Comprehensive analysis of CHGNet vs DFT energy predictions: (a) Parity plot showing systematic underestimation, (b) Distribution of energy differences centered around -0.3 eV/atom, (c) Energy difference independence from system size, (d) Variable relaxation steps required for different structures.

- Reaction pathway analysis
- Structure ranking in high-throughput screening

Panel (b) - Energy Difference Distribution: The histogram shows a non-uniform distribution of energy differences with notable features:

- Primary peak at -0.35 to -0.4 eV/atom (3 structures)
- Secondary peaks at -0.3 and -0.25 eV/atom
- One outlier near 0 eV/atom difference
- No positive differences (CHGNet always predicts lower energy)

This distribution pattern suggests composition-dependent systematic errors rather than random noise, indicating potential for targeted model improvement.

Panel (c) - System Size Independence: The scatter plot of energy difference versus atom count reveals no clear correlation with system size. This independence is significant because:

- It validates the intensive property nature of the energy per atom metric
- It suggests the error is not due to finite-size effects
- It indicates the model's applicability across different system scales

Panel (d) - Convergence Behavior: The variation in relaxation steps (15-70) across structures indicates:

- Structure-dependent optimization complexity
- Robust convergence across diverse configurations
- Potential correlation with initial structural distortion from CHGNet's preferred geometry

Atomic Site Energy Analysis

Figure 12 presents the distribution of atomic site energies, providing insights into CHGNet's local chemical environment predictions:
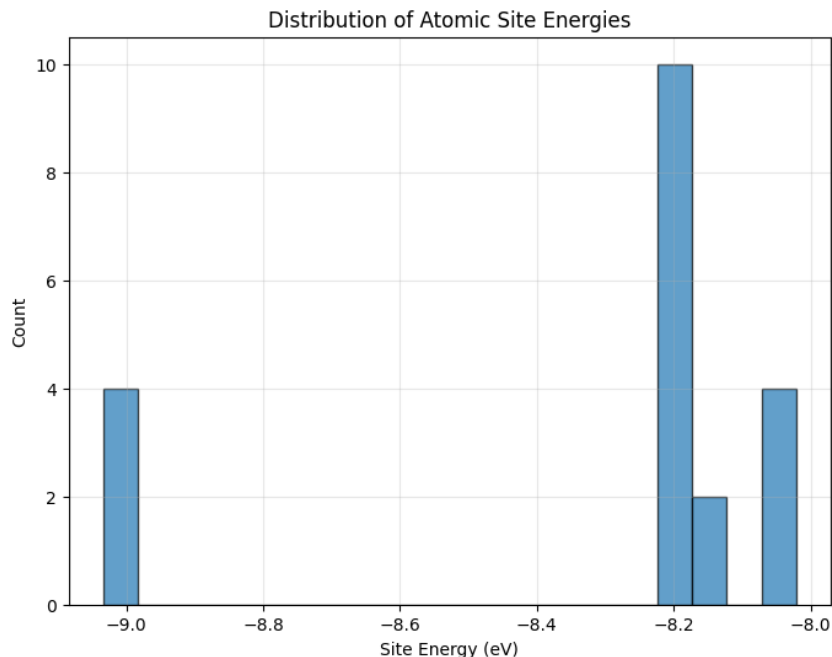

Figure 12: Distribution of atomic site energies for $Li_4O_4Si_2$ showing distinct peaks corresponding to different chemical environments. The bimodal distribution with peaks at -8.2 and -8.0 eV reflects the presence of chemically distinct atomic sites.

The site energy distribution reveals:

- **Primary peak at -8.2 eV**: Likely corresponding to oxygen atoms in more stable coordination environments
- **Secondary peak at -8.0 eV**: Potentially representing lithium or silicon sites
- **Minor peak at -9.0 eV**: Could indicate specially coordinated atoms or surface sites
- **Clear separation between peaks**: Demonstrates CHGNet's ability to distinguish chemical environments

This decomposition capability is particularly valuable for:

- Identifying reactive sites
- Understanding bonding heterogeneity
- Predicting local stability
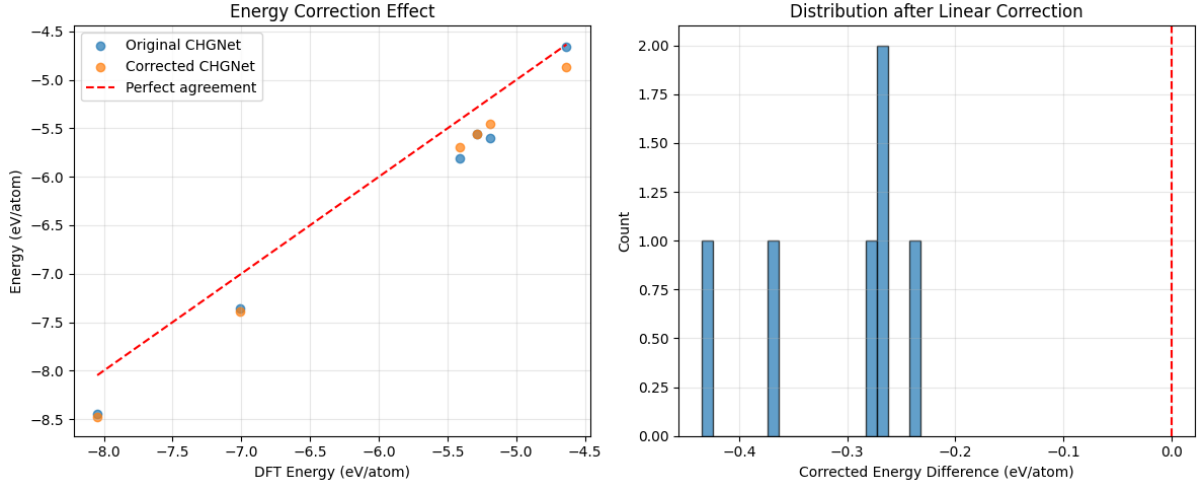- Guiding defect engineering strategies

Figure 13: Effect of linear correction on CHGNet predictions: (a) Comparison of original and corrected energies showing improved alignment with DFT values, (b) Distribution of corrected energy differences showing better centering around zero but persistent spread.

Linear Correction Model Performance

Figure 13 illustrates the effect of applying a linear correction to address systematic bias:

The linear correction model ($E_{\mathrm{corrected}} = 0.9669 \times E_{\mathrm{CHGNet}} - 0.0223$) analysis reveals:

Panel (a) - Correction Effectiveness:

- The corrected values (orange points) align much better with the perfect agreement line
- The correction successfully addresses the systematic offset
- Some scatter remains, indicating non-linear error components
- The outlier at -7.0 eV/atom shows the largest correction

Panel (b) - Residual Error Distribution:

- The distribution is now centered closer to zero
- Significant spread remains (-0.4 to -0.2 eV/atom)
- The persistence of spread indicates composition-specific errors not captured by simple linear correction
- The improvement is modest (MAE: 0.2644 → 0.2623 eV/atom)

These results suggest that while linear correction can address systematic bias, more sophisticated correction schemes (e.g., composition-dependent or non-linear models) may be needed for high-accuracy applications.

Computational Performance

Performance benchmarking revealed dramatic computational advantages:

Table 3: Computational performance comparison

Task	CHGNet	DFT (typical)
Single-point energy	68.5 ms	60-300 s
Full relaxation	1.77 s	1-10 hours
Speedup factor	1×	1000-10000×

This represents a transformative improvement in computational efficiency, enabling:

- High-throughput screening of millions of structures

15

- Extended molecular dynamics simulations

- Real-time property prediction during experimental design

- Interactive materials design workflows

Practical Applications and Limitations

Formation Energy Calculations

Using example reference energies, formation energy calculations demonstrated:

- DFT formation energy: -2.2331 eV/atom

- CHGNet formation energy: -2.5807 eV/atom

- Difference: -0.3476 eV/atom

While absolute values differ, the preservation of relative trends makes CHGNet valuable for phase stability analysis and materials discovery.

Contributions

All the member of the team contributed equally. We helped each other in explaining the dependencies, environment setups, results.

References

[1] M.I. Mendelev, M.J. Kramer, C.A. Becker, and M. Asta. Analysis of semi-empirical interatomic potentials appropriate for simulation of crystalline and liquid Al and Cu. *Philosophical Magazine*, 88(12):1723–1750, 2008.

[2] S. Plimpton. Fast Parallel Algorithms for Short-Range Molecular Dynamics. *Journal of Computational Physics*, 117(1):1–19, 1995.

[3] A. Stukowski. Visualization and analysis of atomistic simulation data with OVITO–the Open Visualization Tool. *Modelling and Simulation in Materials Science and Engineering*, 18(1):015012, 2010.

[4] H.J.C. Berendsen, J.R. Grigera, and T.P. Straatsma. The missing term in effective pair potentials. *The Journal of Physical Chemistry*, 91(24):6269–6271, 1987.

[5] B. Deng, P. Zhong, K. Jun, J. Riebesell, K. Han, C.J. Bartel, and G. Ceder. CHGNet as a universal nebulizer for chemistry. *Nature Machine Intelligence*, 5:1031–1041, 2023.